Effect of heat treatment on corrosion resistance of DMLS AlSi10Mg alloy

M. Cabrini[a,], S. Lorenzi[a], T. Pastore[a], S. Pellegrini[a],*
E.P. Ambrosio[b], F. Calignano[b], D. Manfredi[b], M. Pavese[c], P. Fino[b,c]

[a] DISE-University of Bergamo, Dalmine (BG), Italy
[b] Center for Space Human Robotics@Polito, IIT, Torino, Italy
[c] DISAT - Politecnico di Torino (TO) Italy

Abstract
The paper deals with the effect of heat treatments on corrosion resistance of an AlSi10Mg alloy obtained by means of Direct Metal Laser Sintering. The tests were performed on as-processed alloy and after different post-heat treatment, covering stress relieving, annealing at high temperature and water quenching.
Potentiodynamic and electrochemical impedance spectroscopy tests were carried out in aerated Harrison solution. The results show localized corrosion and selective penetrating attack at the border of melt pools on untreated or only stress relieved specimens. The selective attack was not observed after high temperature annealing. Modification of EIS plot evidenced galvanic coupling with silicon coarse particles that extensively precipitate during high temperature annealing. The morphology of precipitates is described in order to evidence their relevance in terms of rising selective penetrating attack and galvanic coupling.

Keywords: Additive Manufacturing, Direct Metal Laser Sintering, Corrosion, AlSi10Mg, passivity film

1. Introduction

Direct Metal Laser Sintering (DMLS) is an additive manufacturing technology for fabrication of semi-finished parts directly from computer-aided design modelling, through melting and consolidation, layer upon layer, of a metallic powder with a laser source. In comparison to conventional technologies like die-casting, it offers several benefits such as constructing previously impossible geometries thus opening new ways to design; significantly reducing material waste by using only the material necessary; reducing time to market; moving to mass customization [*1*].
The objects fabricated with this technology have specific features. They have rough surfaces and can contain porosities [*2*]. Furthermore, the local fusion of overlapped layers of metallic powder creates small "melt pools" that rapidly solidify with a characteristic fine microstructure, which increases the mechanical properties [*3*] [*4*], but may have adverse effect on corrosion behaviour. A decrease in corrosion resistance of Al-Si alloys produced by DMLS was already evidenced in previous works [*5*] [*6*]. The process produces preferential path for insurgence of selective attacks along the border of melt pool and promotes growth of a passive film less protective than in air formed one. The localized attacks were ascribed to variations of microstructure and chemical composition in the thermal altered zone, inside the melt pool. Although the microstructure is too fine for SEM-EDS analysis, it was hypothesized that thermal cycle due to the laser scans leaves a different alloying element distribution between the border and the centre of the melt pools.
The DMLS process leaves high residual thermal stresses in metal structure. In order to reduce them and avoid distortion of the object, stress relieving is usually adopted [*7*]. More pronounced modifications in microstructures of alloys produced by DMLS can be achieved by annealing at higher temperature, as shown by Aboulkhair et al on AlSi10Mg [*8*], Prashanth et al on Al-12Si alloy [*9*], and Pan Ma et al on Al-20Si alloy [*10*]. However, some works were published on the microstructure of Al-Si-Mg cast alloys [*11*] [*12*].

Heat treatments at high temperature can promote the coalescence of second phases and change their distribution [*13*]. In addition, the presence of intermetallics containing impurity of iron and copper, which promote selective attacks, can be favoured.
The paper deals with the effect of heat treatments on corrosion resistance of an AlSi10Mg alloy obtained by means of DMLS. It investigates the effectiveness of microstructure modifications by high temperature heat treatment for restoring the intrinsic corrosion resistance of the alloy.
The corrosion resistance is evaluated in aerated Harrison solution at room temperature by means of potentiodynamic tests and Electrochemical Impedance Spectroscopy (EIS). The tests were executed both on as produced surface and after polishing in order to assess the effect of the film formed during fabrication process.

2. Experimental

The tests were carried out on specimens obtained by DMLS using a gas atomized AlSi10Mg powder produced by EOS (Germany). Table 1 reports the chemical composition of the alloy. Near eutectic Al-Si alloy is commonly used in casting due to its low melting temperature, around 843 K. Further details about powder composition, grading and other specifications are reported in previous works [*7*] [*14*]. The particles have quite regular spherical shape, ranging from 0.5 to 40 μm, with a mean size of 25 μm.
During DMLS process, the laser beam intensity was adjusted in order to achieve partial melting between adjacent powder layers to grant a good jointing. The direction of scanning was rotated by 67° between consecutive layers in order to achieve the best densification [*14*]. The scan speed, laser power and hatching distance were optimized in order to minimize porosities, as previously reported [*7*]. The role of scan strategy to reduce the porosity of specimens was also underlined by Aboulkhair et al [*15*], Read et al [*16*], and Louvis et al [*17*].
Disk specimens with 15 mm diameter and 5 mm height were used. They were produced by considering the base circular face parallel to the building platform. The specimens as obtained by DMLS process without any further heat treatment are called untreated (UT).
The relieving of residual stresses was performed in furnace at 573 K for 2 h on specimen still placed on the building platform. Such specimens were named SR (Stress Relieved).
In order to achieve more pronounced modifications of microstructure and homogeneous distribution of alloying elements, a solution annealing treatment at 823 K for 4 hours followed by water quenching (WQ) was carried out at the upper temperature limit for this type of heat treatment, after stress relieving.
Two different surface conditions were considered. The tests were performed on the rough surface as-produced by DMLS (AP) and after polishing (P) by emery paper and 0.1 μm alumina. The polished specimens remained at air for 48 hours before corrosion tests. All specimens were degreased with acetone in ultrasonic bath.
The microstructure of specimens was observed at the optical microscope and scanning electron microscope (SEM) equipped with energy dispersive X-ray detector (EDS). The specimens were polished with emery papers up to 4000 grit and 0.1 μm alumina suspension. The metallographic etching was carried out by means of Keller's reagent. Vickers micro-hardness tests were executed by using 100 g load and 15 seconds loading time.
Corrosion tests were carried out at room temperature in aerated Harrison's solution (3.5 g/L of $(NH_4)_2SO_4$, 0.5 g/L di NaCl, pH 5.5). All the tests were repeated at least twice. The electrochemical tests were performed in one litre ASTM G5 standard cell by using a specimen holder with 1 cm^2 exposed area, a standard calomel reference electrode (SCE) and two graphite counter electrodes. Potentiodynamic tests were carried out at 0.001 V/s scan rate from -0.050 V respect to free corrosion potential (E_{cor}) until the anodic current density reaches 10 mA/cm^2. Before tests, the open circuit potential was monitored for 30 minutes. Free corrosion potential was measured during tests up to 160 hours' exposure. Electrochemical impedance spectroscopy (EIS) tests were carried out only on

polished specimens every 10 hours. Signal with 0.010V amplitude in the frequencies range between 10 kHz and 10^{-2} Hz was applied.
At the end of the tests, the specimens were firstly washed with distilled water, then rinsed with acetone in ultrasonic bath and finally dried. Corrosion morphologies were observed by means of optical and scanning electron microscopes.

3. Results and discussion

3.1 Microstructure

Figure 1 shows the structure of UT and SR specimens. The macrostructure shows tracks of the laser scanning during the manufacturing process. Because the melting occurs in powder layers forming small melt pools, which rapidly solidify, the resulting solid microstructure achieves directional growth features far from equilibrium. Over the powder deposition plane, the melt pool contour lines create irregular geometric contours reflecting the changes of laser scan directions of consecutive layers (Figure 1a and b).
Along z-direction, which is the building direction of the specimens, the macrostructure shows trace of powder deposition plane, with melt pools having the characteristic semi-circular section, placed over previous tracks (Figure 1c and d). The underlying metal, which is only superficially melted, quickly removes the heat from the liquid and guarantees the adhesion of the track to the substrate. Each singular track could be considered as a small cast laid on the previous one.
The microstructure does not show relevant modifications after stress relieving heat treatment at 573 K, whereas annealing at 823K gives rise to a matrix of α-Al phase with inside rounded silicon precipitates (Figure 2) varying from 1 to 10 μm, described by Ogris et al. [*18*].
Table 2 summarizes the micro-hardness results. The data confirm that the very fine microstructure after DMLS process is associated to high hardness. Compared with SR specimens, the annealing heat treatment leads to a softening.

3.2 Potentiodynamic tests

Figures 3 and 4 show the potentiodynamic curves on AP and P surfaces. The curves have two different behaviours, one with well-defined passive range - which is upper limited by pitting potential (E_p) - and the other almost active above free corrosion potential. Table 3 matches the values of free corrosion potential and pitting potential derived by potentiodynamic curves. Pitting potentials are very scattered, whereas free corrosion potential is usually around -0.62 V vs SCE.
Figure 5 summarizes the influence of heat treatment on the pitting potentials. The AP specimens show an almost active behaviour independently upon the heat treatment. On P specimens, the temperature of the heat treatment significantly affects the corrosion behaviour. Thus, WQ specimens show a marked decrease of the pitting potential compared to either UT or SR specimens, approaching typical values of free corrosion potentials of almost active behaviour.
The pitting potential results reflect both the intrinsic quality of passive film and microstructure. The curves obtained on the AP surface always had anodic current densities higher than P surfaces. The increasing of the current density can be ascribed to the roughness of the AP surface, which increases the real exposed area. However, heat treatments can significantly modify the passive film nature. The thermally formed oxide during DMLS fabrication and subsequent heat treatments is less protective compared to natural oxide. Thus, the weakness of thermally formed films promptly led to the initiation of localized attack during early ages of immersion, giving the almost active behaviour observed in the potentiodynamic tests.
Vargel reported that the natural oxide film of aluminium is built up from two superimposed layers with a total thickness between 4 and 10 nm. The inner barrier film - compact and amorphous - quickly forms at any temperature as soon as the metal comes in contact with air. The kinetic does not depend

upon the oxygen partial pressure and the temperature acts only on the final thickness. The second layer grows on the barrier layer by hydration reaction. Its final thickness is reached only after several weeks - even months - and it depends on the physicochemical conditions. Thermal heat treatments modify the passive film morphology. They increase layer thickness and crystallinity of the oxide, but they produce porous and micro-cracked structure, which have lower corrosion resistance compared to the amorphous film [*19*].

The results on AP specimens suggest a major effect of poor protective film on the corrosion behaviour and only a minor or negligible effect of alloy microstructures.

On the P specimens, the film formed during DMLS process and subsequent heat treatment was removed by grinding. Under these circumstances, the modification of microstructures can produce major effects on the anodic electrochemical behaviour. However, the film formed during DMLS process cannot be completely removed inside the emerging porosities. These sites act as preferential zones for localized attacks initiation. Actually, on the UT and SR specimens, attacks only initiated inside the residual porosity, where the film formed during DMLS was still present (Figure 6a). Thus, the scattering of the corrosion and pitting potentials can be explained by considering the statistical distribution and size of emerging porosities formed during the fabrication process.

On UT and SR specimens, the attack takes place by selective dissolution of the α-Al phase, preferentially along the border of the melt pools (Figure 6b).

Annealed specimens behave differently and show practically uniform dissolution of α-Al phase. Corrosion occurs without any deep penetrating dissolution, leaving an enrichment of silicon particles on the surface. The selective attack at the border of melt pool was not observed due to the more homogeneous microstructure obtained after annealing, but the more homogeneous distribution of the silicon particles significantly decreases the corrosion resistance of the passive film, producing practically active behaviour.

3.3 EIS tests

EIS spectrum was measured every 10 hours, up to 160 hours of immersion in the Harrison solution. The tests were only carried out on polished specimens. The EIS curves have been obtained on polished specimens, in order to evidence the effect of microstructure and heat treatments. The protectiveness of the passive film formed on the alloy surface with different finishing was reported in a previous work by authors [*6*]. The free corrosion potential during EIS monitoring is shown in Figure 7. Some variations over time can be underlined. Potential values just after immersion are close to those measured before potentiodynamic tests. The potential varies over time especially for UT specimens, with an increase of about 0.15V during early time. Afterwards, a stabilization around -0.60 V vs SCE was noticed on UT and SR specimens, at longer exposures. The potential of WQ specimens stabilizes around -0.7V vs SCE, denoting a prevalent anodic reactivation.

Figures from 8 to 10 show the modification of EIS curves over time. The values at high frequency represent the ohmic drop in the electrolyte, which remains almost constant in all the tests.

Several differences can be evidenced in the middle-low frequencies range between the specimens with different heat treatments. Initially, UT and SR specimens evidence a typical behaviour of passive aluminium. The bode-phase diagram is characterized by a wide peak – which appears non-symmetric for SR condition - in the frequency range between 10^2 and 10^{-1} Hz. Such broad peak derives from the superposition of two different peaks with non-distinguishable time constants. Just after immersion, UT specimens show very high impedance values at low frequency, in the order of magnitude of million ohm cm^2, close to the values observed on SR specimens.

WQ specimens show a different behaviour compared to UT and SR specimens. Just after immersion, the modulus of impedance at low frequency is about two order of magnitude lower than UT and SR specimens. Moreover, two well defined time constants in the intermediate frequency range can be noticed. The lower impedance modulus at low frequencies is in accordance with the active behaviour observed during potentiodynamic tests on polished specimens. On the contrary, the passive behaviour

observed for UT and SR specimens can be associated with the high impedance modulus at low frequency.
The behaviour changes over time, with modifications that are far more evident for UT and SR specimens rather than WQ specimens. The initial broad peak in the Bode phase diagrams separates into two partially overlapped peaks, typical of an equivalent circuit having two time constants in this frequency range. The impedance modulus decreases by an order of magnitude at longer exposure. The time needed for two time constants appearance depends upon the heat treatment. UT condition shows two overlapped peaks up to 58 hours' exposure and the two peaks are only well defined at 164 hours. The two peaks behaviour is evident on SR specimens since early exposure, but they become far more evident after 60 hours. The peaks subdivision can be easily noticed since early exposure of WQ specimens, and the peaks amplitude is even lower compared to UT and SR. However, it must be underlined that the frequencies of the phase peaks remain constant at 150-400 Hz and 0.1-1Hz for all the testing conditions, independently upon heat treatment.

3.4 Microstructure and EIS spectra

The time evolution of the EIS spectra reveals the microstructure of the alloy and the corrosion phenomena that modifies the characteristics of the exposed surface, directly in contact with the testing solution.

For UT specimens, the phase plot typical of passive conditions remains for longer period compared to heat-treated specimens. The double-peak behaviour can only be noticed at prolonged exposures, but peaks are not well defined. WQ specimens showed well defined and separate peaks since early exposures. SR specimens exhibit intermediate behaviour. The double-peak behaviour is well evidenced after shorter exposure compared to untreated specimens and it is far more pronounced.

The microstructure of annealed specimens is characterized by coarse silicon particles. On the surface, therefore, rather large area of emerging silicon particles forms galvanic couples with surrounding aluminium areas. The presence of such dissimilar areas gives two time constants response in EIS plot. The dual conformation of the surface determines the appearance of the second peak. It is well recognized that silicon is cathodic with respect to the α-Al phase matrix, which may lead to the formation of micro-galvanic couples resulting in localized corrosion phenomena [*20*] [*21*]. The higher nobility of the silicon particles than the α-Al phase was directly evaluated by means of Scanning Probe Microscopy [*22*]. Osòrio et al. underlines the increase of corrosion rate of cast Al-Si alloy by increasing the silicon content [*23*].

The galvanic coupling tends to reactivate the surface of the aluminium. The initiation of localized corrosion changes the impedance of the passive aluminium, but it maintains the dual nature of the surface. According to the results of potentiodynamic tests, the corrosion morphology of annealed specimens is large pit (Figure 11a) uniformly distributed on the whole surface. Over the time, corrosion enhances the presence of non-dissolving silicon particles on the metal surface. Afterwards, the increase of emerging silicon area can modify the impedance response after long-time exposure, causing slight increase of the values of impedance modulus at low frequency.

The microstructure of untreated specimens only shows a reduced precipitation of very fine α-Al-silicon eutectic, mainly distributed along the border of aluminium dendrites. Isolated silicon particles are present inside the melt pool borders. The exposed surface of such particles is much lower than in annealed specimens and no modification of the impedance response just after immersion are evidenced. Their fine dimensions and extension - much lower than the coarse silicon particles produced by high temperature heat treatments - do not produce early modification in EIS plot, but their unique morphology causes the penetrating selective attack (Figure 11b) to occur along preferential path at the melt pool boundaries, similarly to that observed after the potentiodynamic tests. The EDS analysis was not able to distinguish the composition of the individual particles, as

matter of fact their size was too small compared to the beam dimension. However, an enrichment of silicon and oxygen in correspondence of the etched areas was found [*24*].

Stress relieving also promotes silicon precipitation and coarse silicon particles, but their size remains significantly lower than after high temperature annealing heat treatment. Stress relieving does not alter the microstructure along the melting pool – as annealing does – and selective attack is still present on SR specimens, as a consequence.

The microstructure of UT and SR specimens evidences differences in distribution of silicon particles between the centre and the border of the melt pools and the HAZ. In the HAZ, the silicon particles are isolated and larger than those inside the melt pool (Figure 6). In this zone the microstructure is similar to the microstructure of the annealed specimens, but the dimension of the particles is finer.

Figure 12 shows the selective corrosion of α-Al phase near the silicon particles in WQ specimens, causing the detachment of the silicon particles. As the corrosion attack becomes deeper, coalescence of attacks can be noticed. Owing to the greater concentration of silicon particles along the former border rather than in the centre of the melt pool, the attack tends to follow this path.

Similar conditions have been detected in the HAZ of UT and SR specimens, where localized attacks preferentially grow along the border of the melt pool. The presence of idiomorphic silicon crystals, which can act as preferential cathode but not as physical barrier on the α-Al phase, explains the selective attack in the HAZ. The α-Al phase dissolves also inside the melt pool, but slowly than in the HAZ, owing to the silicon network that hinders the aluminium grains and anchors the aluminium oxide, avoiding the diffusion of corrosion products from within attacks towards the bulk of solution. UT and SR conditions characterized by higher pitting potentials and higher values of EIS impedance modules at low frequency, showed also longer time to separation of time constants in the Bode phase diagrams. This could be ascribed to the quality of the passive film formed, strictly connected with silicon particles distribution.

3.5 EIS spectra fitting and modelling

The equivalent circuit model able to physically describe the complexity of corrosion phenomena on DMLS alloy should take into account the three different mechanisms that take place over time concerning passive zones, localized corrosion areas and regions of selective penetrating attack further enhanced by silicon particles morphology and distribution. Just after immersion - when aluminium is passive or localized corrosion occurs - a circuit like that proposed by Mansfeld et al. [*25*] and Bessone et al. [*26*] could be suitable to explain the corrosion behaviour and accurate fitting of EIS spectra can be obtained. However, in presence of the selective penetrating attack, a second well defined peak at low frequencies can be noticed, and a second time constant clearly arise.
An equivalent circuit that takes into account all the processes should be constituted by a parallel of elements, one for passive aluminium – far from silicon particles rich zones – one for the aluminium active areas near silicon particles and a last one for the silicon particles itself. The equivalent circuit for the aluminium DMLS alloy becomes very complex – beyond of the aims of this work - and too large number of variables are involved in the fitting of the impedance curves.
The simplest way to interpret and correlate the modifications of corrosion morphologies to EIS spectra is to evidence the evolution of time constants. Thus, for the aim of this work, which is mainly devoted to the modification of corrosion behaviour by heat treatments, a model based on a simplified equivalent circuit (SEC) is convenient for describing impedance curve modification during exposure. The simplified equivalent circuit (Figure 13) consists of series of a resistance (Rs) representing the ohmic drop in the electrolyte and two resistance/constant phase element parallels (Z1 and Z2) describing the two different frequency responses.

The simplified serial equivalent circuit can be conveniently used to evidence the time-to-corrosion attack occurrence, in terms of modification of peaks frequencies and separation of the two time constants.
Figure 14 shows – as a title of example - the fitting of EIS curves obtained by the application of SEC to experimental data of WQ specimens, with well-defined two peaks behaviour. The circuit fit very well the experimental data, with a clear identification of the peaks. The modification of the time constants obtained by means of simplified equivalent circuit as a function of exposure time is shown in Figure 15. The time constants are defined as the product of capacitance and resistance of the Z1 and Z2 elements and they are named τ_1 and τ_2, respectively. Two well-defined zones can be evidenced, one in the 1-10 seconds range, and the other in the 10^{-1}-10^{-4} seconds range. The peak at low frequency is relative to Z1 element, and the peak at high frequency is relative to the Z2 element. τ_1 is almost the same for all the heat treatments. τ_2 changes by orders of magnitude moving from UT and SR to WQ, just after immersion. The time constant modifies over exposure and the time-to-subdivision is longer for UT specimens, whilst SR and WQ specimens show a subdivision since early exposure. At long exposures, the time constants of UT and SR specimens are practically coincident. On the contrary, the τ_2 time constant of WQ specimens is significantly lower over the whole exposure time. When localized corrosion or penetrating attack occurs, τ_2 reduces.
Consequently, it is possible to relate τ_2 time constant to the dissolution of the α-Al phase close to silicon particles, which macroscopically occurs on annealed specimens and microscopically - at the boundaries of the melt pools - during the selective attack. The size of silicon particles and more uniform distribution of WQ can enhance general corrosion of the aluminium matrix and τ_2 time constant is the lowest.

4 Conclusions

Potentiodynamic and EIS tests were carried out on AlSi10Mg alloy manufactured by means of DMLS with different post-heat treatments.
The results confirm the formation during DMLS of a passive film less protective than that spontaneously formed in air and evidence the presence of localized attack and penetrating selective attack at the border of the melt pools, due to the characteristic precipitation morphology of silicon phases.
The low temperature heat treatment for two hours at 573 K usually performed for relieving residual internal stress derived from fabrication process does not reduce the susceptibility to the penetrating selective attack.
Annealing for four hours at 823K promotes the coalescence of silicon particles. Consequently, EIS spectra modifies denoting a clear galvanic coupling between emerging coarse silicon particles and surrounding aluminium matrix. Localized corrosion evolves, but without any penetrating selective attack.

References

1 Frazier, W.E. Metal Additive Manufacturing: A Review. *Journal of Materials Engineering and Performance*, 23, 6 (2014), 1917-1928.

2 Liu, A., Chua, C.K., and Leong, K.F. Properties of test coupons fabricated by selective laser melting. *Key Engineering Materials*, 447-448 (2010), 780-784.

3 Calignano , F., Manfredi , D., Ambrosio , E.P., Iuliano , L., and Fino, P. Influence of process parameters on surface roughness of aluminum parts produced by DMLS. *International Journal of Advanced Manufacturing Technologies*, 67 (2013), 2743–2751.

4 Thijs, Lore, Kempen, Karolien, Kruth, Jean-Pierre, and Van Humbeeck, Jan. Fine-sructured aluminium products with controllable texture by selective laser melting of pre-alloyed AlSi10Mg powder. *Acta Materialia* , 61 (2013), 1809-1819.

5 Cabrini, Marina, Lorenzi, Sergio, Pastore, Tommaso et al. Evaluation of corrosion resistance of Al–10Si–Mg alloy obtained by means of Direct Metal Laser Sintering. *Journal of Materials Processing Technology*, 231 (2016), 326-335.

6 Cabrini, M., Lorenzi, S., Pastore, T. et al. Corrosion resistance of direct metal laser sintering AlSiMg alloy. *Surface and Interface Analysis* (2016).

7 Manfredi, D., Calignano, F., Ambrosio, E.P. et al. Direct Metal Laser Sintering: an additive manufacturing technology ready to produce lightweight structural parts for robotic applications. *La metallurgia italiana* , 105, 10 (ottobre 2013), 15-24.

8 Aboulkhair , N.T., Tuck , C.J., Ashcroft , I., and Maskery , I. On the Precipitation Hardening of Selective Laser Melted AlSi10Mg. *Metallurgical and Materials Transactions A* , 46, 8 (2015).

9 Prashanth, K.G., Scudino, S., Klauss, H.J. et al. Microstructure and mechanical properties of Al-12Si producd by selective laser melting: effect of heat treatment. *Materials Science & Engineering A* , 590 (2014), 153-160.

10 Ma, P., Prashanth, K.G., Scudino, S. et al. Influence of annealing on mechanical porperties of Al-20Si processed by laser melting. *Metals*, 4 (2014), 28-36.

11 Petric, M., Medved, J., and Mrvar, P. Effect of grain refinement, modification and the cooling rate on microstructure of the AlSi10Mg. *RMZ - Materials and Geoenvironment*, 53, 3 (2006), 385-401.

12 Ye, H. An overview on the development of Al-Si-Alloy based material for engine applications. *Journal of Materials Engineering and Performance*, 12 (2003), 288-297.

13 Li, W., Li, S., Liu, J. et al. Effect of heat treatment on AlSi10Mg alloy fabricated by selective laser melting: Microstructure evolution, mechanical properties and fracture mechanism. *Materials Science & Engineering A*, 663 (2016), 116–125.

14 Manfredi, Diego, Calignano, Flaviana, Manickavasagam, Krishnan, Canali, Riccardo, Ambrosio, Elisa Paola, and Atzeni, Eleonora. From powders to dense metal parts: characterization of a commercial AlSiMg alloy processed through direct metal laser sintering. *Materials* , 6 (2013), 856-869.

15 Aboulkhair, N.T., Everitt, N.M., Ashcroft, I., and Tuck, C. Reducing porosity un AlSi10Mg parts processed by selective laser melting. *Additive Manufactoring*, 1, 1-4 (2014), 77-86.

16 Read, N., Wang, W., Essa, K., and Attallah, M.M. Selective laser melting of AlSi10Mg alloy: Process optimisation and mechanical properties development. *Materials and Design*, 65 (2015), 417–424.

17 Louvis, E., Fox, P., and Sutcliffe, C.J. Selective laser melting of aluminium components. *Journal of Materials Processing Technology*, 211, 2 (2011), 275–284.

18 Ogris, E., Wahlen, A., Lüchinger, H., and Uggowitzer, P.J. On the silicon spheroidization in Al–Si alloys. *Journal of Light Metals*, 2, 4 (2002), 263-269.

19 Vargel, C. *Corrosion of Aluminium*. Elsevier Ltd., Oxford, 2004.

20 Arrabal, R., Mingo, B., Pardo, A., Mohedano, M., Matykina, E., and Rodríguez, I. Pitting corrosion of rheocast A356 aluminium alloy in 3.5 wt.% NaCl solution. *Corrosion Science*, 73 (2013), 342-355.

21 Liang, Z.X., Ye, B., Zhang, L., Wang, Q.G., Yang, W.Y., and Wang, Q.D. A new high-strength and corrosion resistant Al-Si based casting alloy. *Materials Letters* , 97 (2013), 104-107.

22 Fratila-Apachitei, L.E., Apachitei, I., and Duszcz, J. Characterization of cast AlSi(Cu) alloys by scanning Kelvin probe force microscopy. *Electrochimica Acta*, 51 (2006), 5892–5896.

23 Osòrio, Wislei R., Goulart , Pedro R., and Garcia, Amauri. Effect of silicon content on microstructure and electrochemical behavior of hypoeutectic Al.Si alloys. *Materials Letters*, 62 (2008), 365-369.

24 Cabrini, M., Lorenzi, S., Pastore, T. et al. Corrosion resistance of Direct Laser Sintering AlSiMg alloy. In *Eurocorr 2014* (Pisa 2014), Dechema, .

25 Mansfeld, F., Lin, S., Kim, S., and Shlh, H. Pitting and Passivation of Al Alloys and Al-Based Metal Matrix Composites. *J. Electrochem Soc.*, 137, 78 (1990).

26 Bessone, J.B., Salinas, D.R., Mayer, C.E., Ebert, M., and Lorenz, W.J. An EIS study of aluminium barrier-type oxide films formed in different media. *Electrochimica Acta*, 37, 12 (1992), 2283-2290.

Table 1: Chemical composition (wt%) of the alloy

Si	Fe	Cu	Mn	Mg	Zn	Ti
10.1	0.16	0.001	0.002	0.35	0.002	0.01

Table 2: Vickers microhardness

Specimens	Stress Relieving			Annealing			$HV_{0.1,15s}$
	T (K)	t (h)	Cooling	T (K)	t (h)	Cooling	
UT	-	-	-	-	-	-	124±4
SR	573	2	air	-	-	-	110±4
WQ	573	2	air	823	1	water	82±3

Table 3: Corrosion and pitting potential by potentiodynamic tests

Heat treatment \ Surface finishing	As Produced (AP)		Polished + 48h air (P)	
	E_{corr} (E vs SCE / V)	E_p (E vs SCE / V)	E_{corr} (E vs SCE / V)	E_p (E vs SCE / V)
UT	-0.561	-0.561*	-0.570	+0.206
	-0.649	-0.649*	-0.758	-0.167
SR	-0.869	-0.547	-0.624	+0.201
	-0.650	-0.592	-0.602	+0.079
	-0.635	-0.610	-0.476	-0.177
	-0.615	-0.615*		
	-0.628	-0.616		
	-0.739	-0.564		
A-WQ	-0.608	-0.608*	-0.620	-0.620*
	-0.600	-0.600*	-0.610	-0.541

*For almost active behaviour, the free corrosion potential was considered as pitting potential

Table captions

Table 1: Chemical composition (% weight) of the alloy

Table 2: Vickers microhardness

Table 3: Corrosion and pitting potential by potentiodynamic tests

Figure captions

Figure 1 Optical images of microstructures of untreated (left) and SR (right) specimen, along building plane (upper) and building direction (lower)

Figure 2 SEM image of the microstructure of WQ specimens with α-Al matrix surrounding coarse silicon particles

Figure 3: Potentiodynamic curves obtained on P specimens with different heat treatments

Figure 4: Potentiodynamic curves obtained on AP specimens with different heat treatments

Figure 5: Pitting potential as a function of heat treatment. Full marks represent P specimens, empty marks represent AP specimens

Figure 6: Localized attack on the UT specimen after the potentiodynamic test in Harrison solution macro image, b) close-up inside the localized attack

Figure 7: Corrosion potential values measured during EIS tests

Figure 8 Effect of exposure time on EIS Bode plots of UT specimens, on P surface, in aerated Harrison solution

Figure 9 Effect of exposure time on EIS Bode plots of SR specimens, on P surface, in aerated Harrison solution

Figure 10 Effect of exposure time on EIS Bode plots of WQ specimens, on P surface, in aerated Harrison solution

Figure 11: SEM images of metallographic section. Corrosion morphology after long exposure in Harrison solution: a) pitting on WQ specimens, b) selective penetrating attack on UT specimen

Figure 12: Corrosion morphology on WQ specimens after 300 hours exposure in Harrison solution

Figure 13 Simplified equivalent circuit suitable to decribe EIS spectra evolution over time

Figure 14: Fitting of experimental data by applying the SEC on WQ specimen

Figure 15: Time constant evolution as a function of exposure time derived from EIS data fitting by means of SEC on a) UT, b) SR, c) WQ specimens

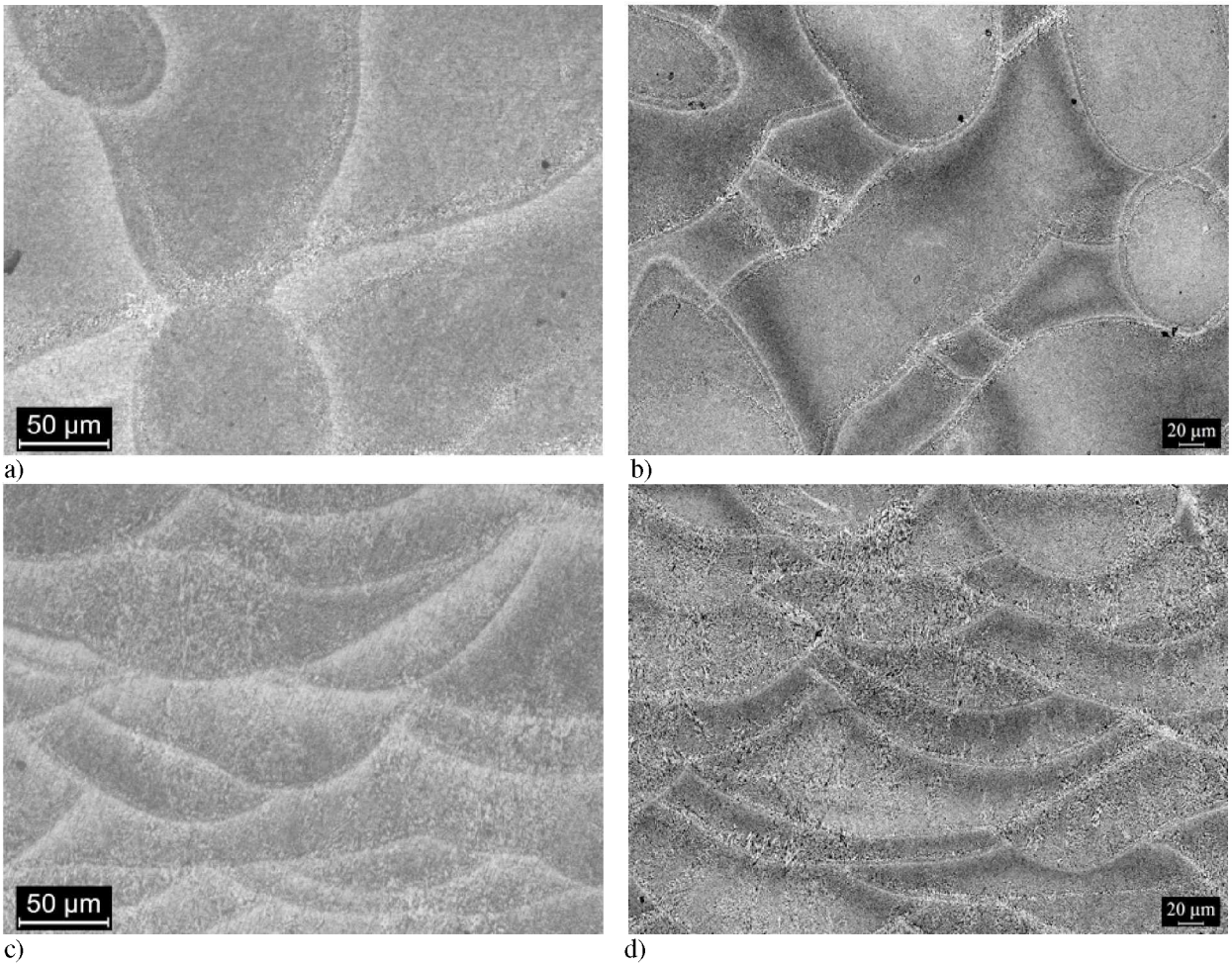

Figure 1 Optical images of microstructures of untreated (left) and SR (right) specimen, along building plane (upper) and building direction (lower)

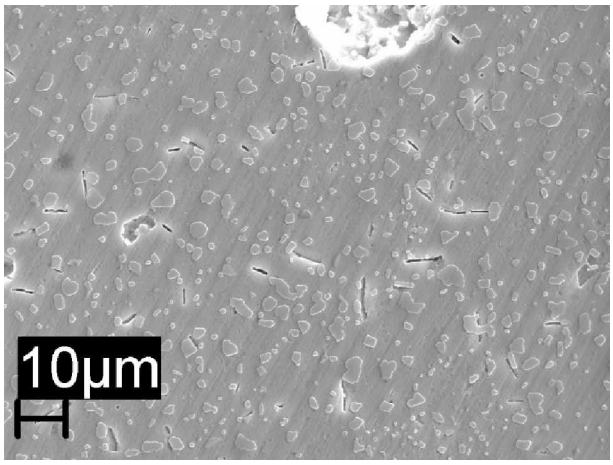

Figure 2 Microstructure of WQ specimens

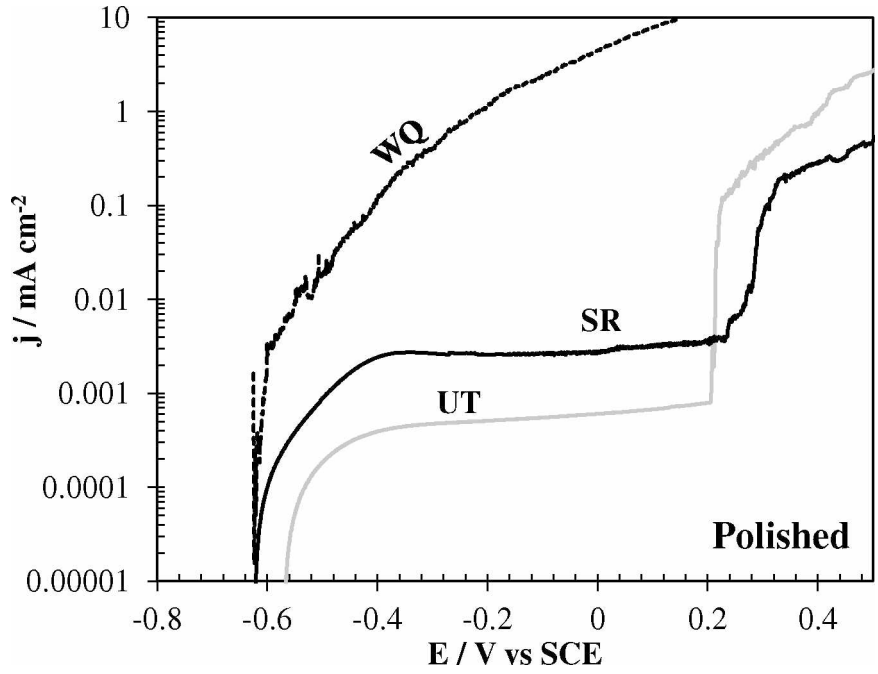

Figure 3: Potentiodynamic curves obtained on P specimens with different heat treatments

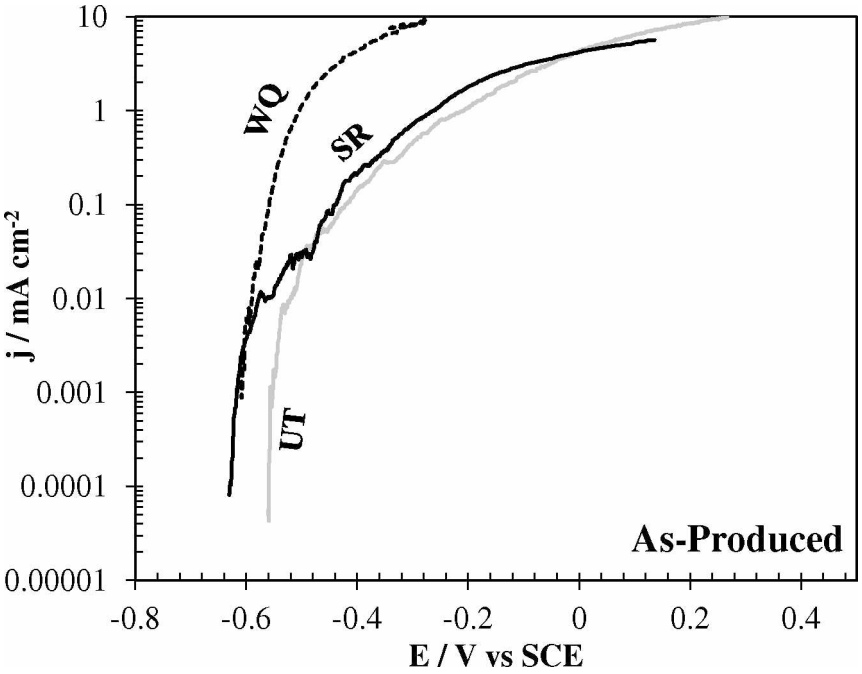

Figure 4: Potentiodynamic curves obtained on AP specimens with different heat treatments

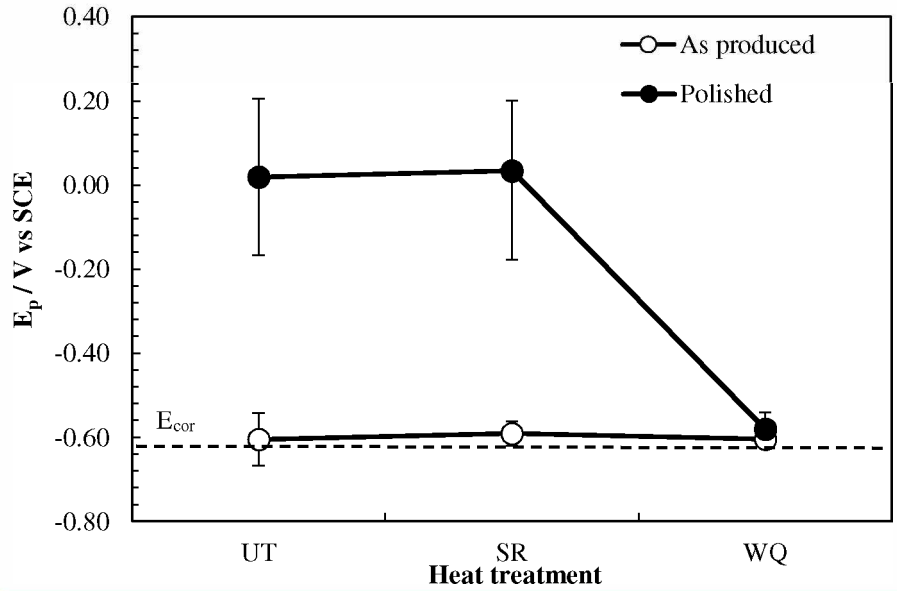

Figure 5: Pitting potential as a function of heat treatment. Full marks represent P specimens, empty marks represent AP specimens

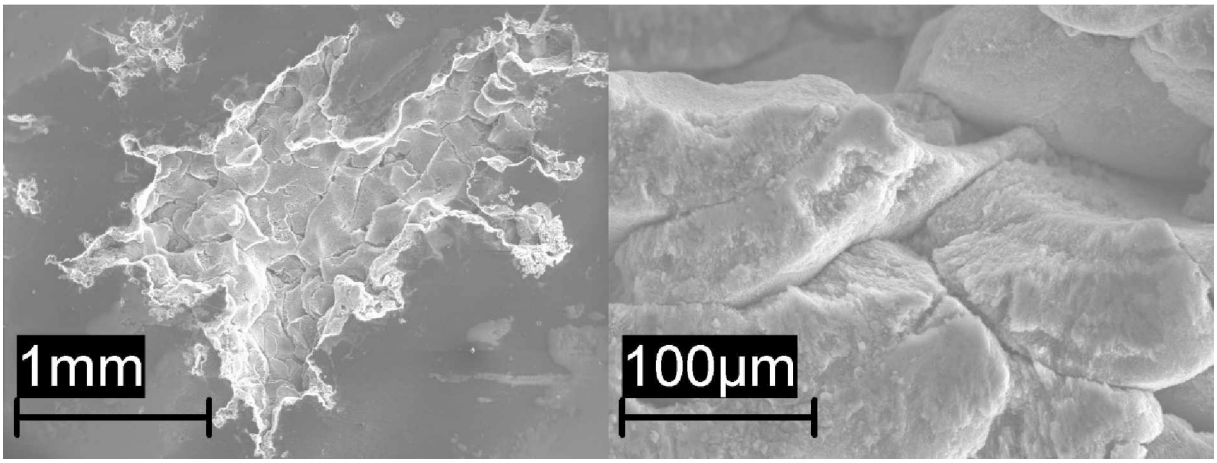

a) b)

Figure 6: Localized attack on the UT specimen after the potentiodynamic test in Harrison solution macro image, b) close-up inside the localized attack

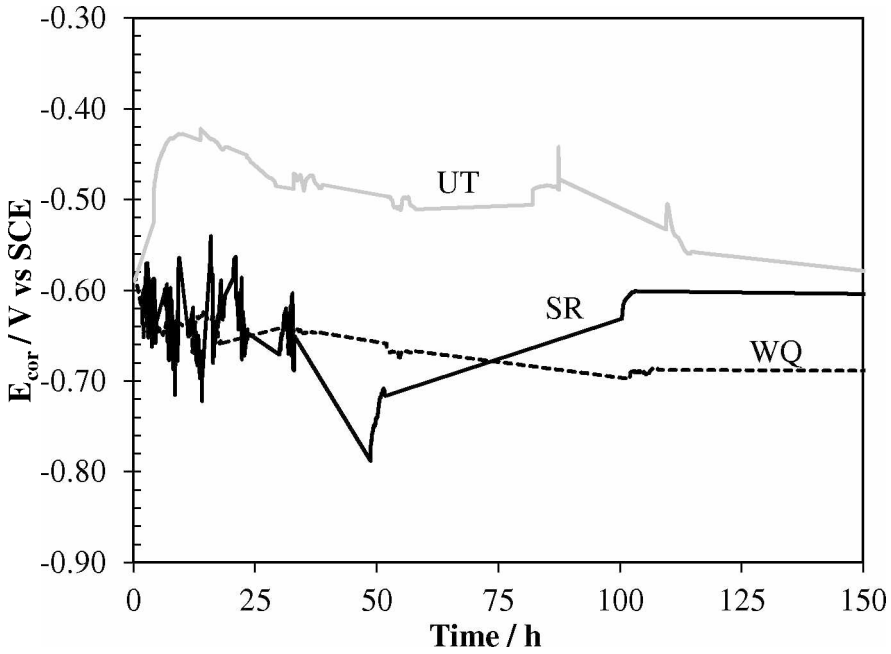

Figure 7: Corrosion potential values measured during EIS tests

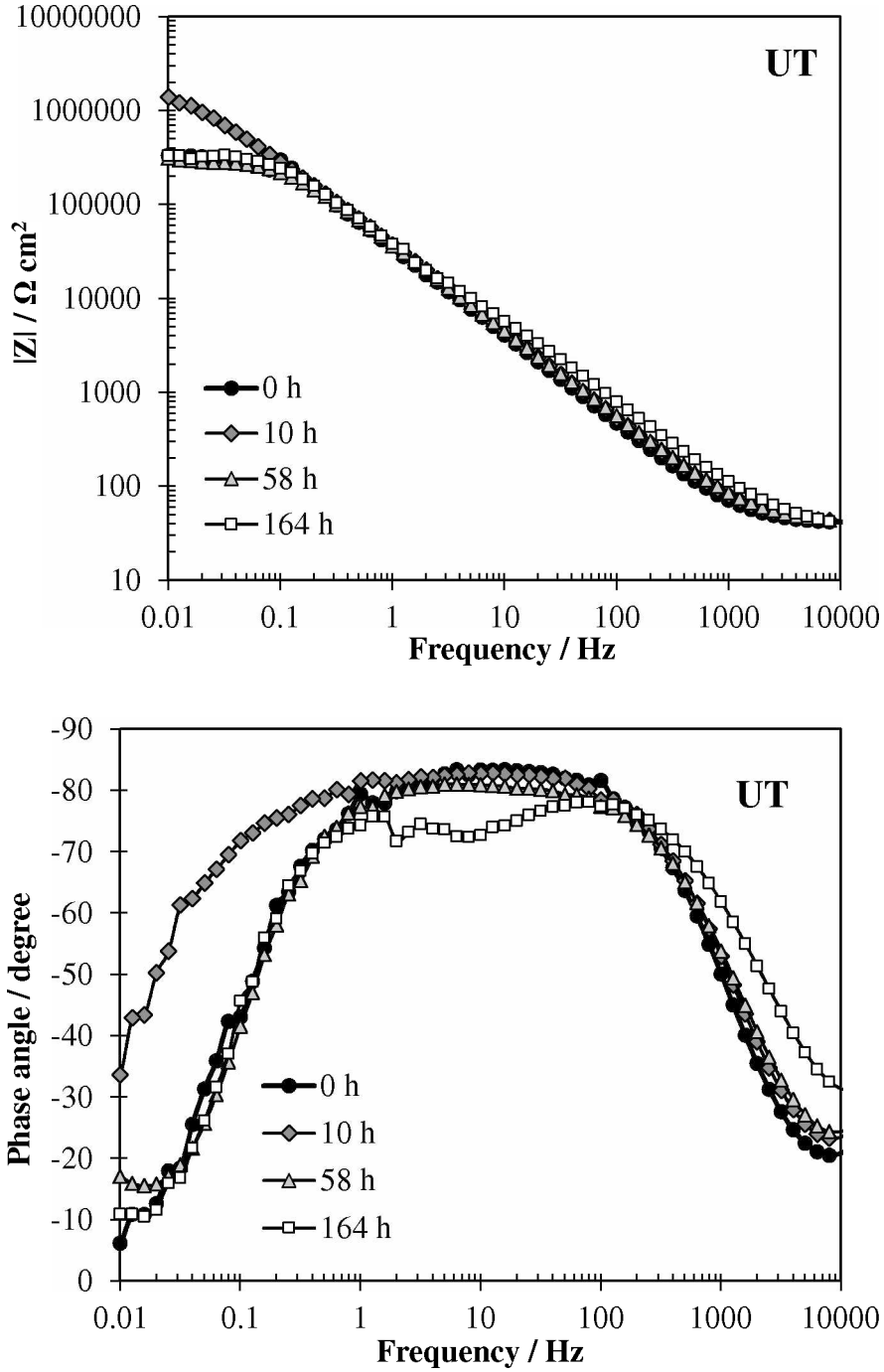

Figure 8 Effect of exposure time on EIS Bode plots of UT specimens, on P surface, in aerated Harrison solution

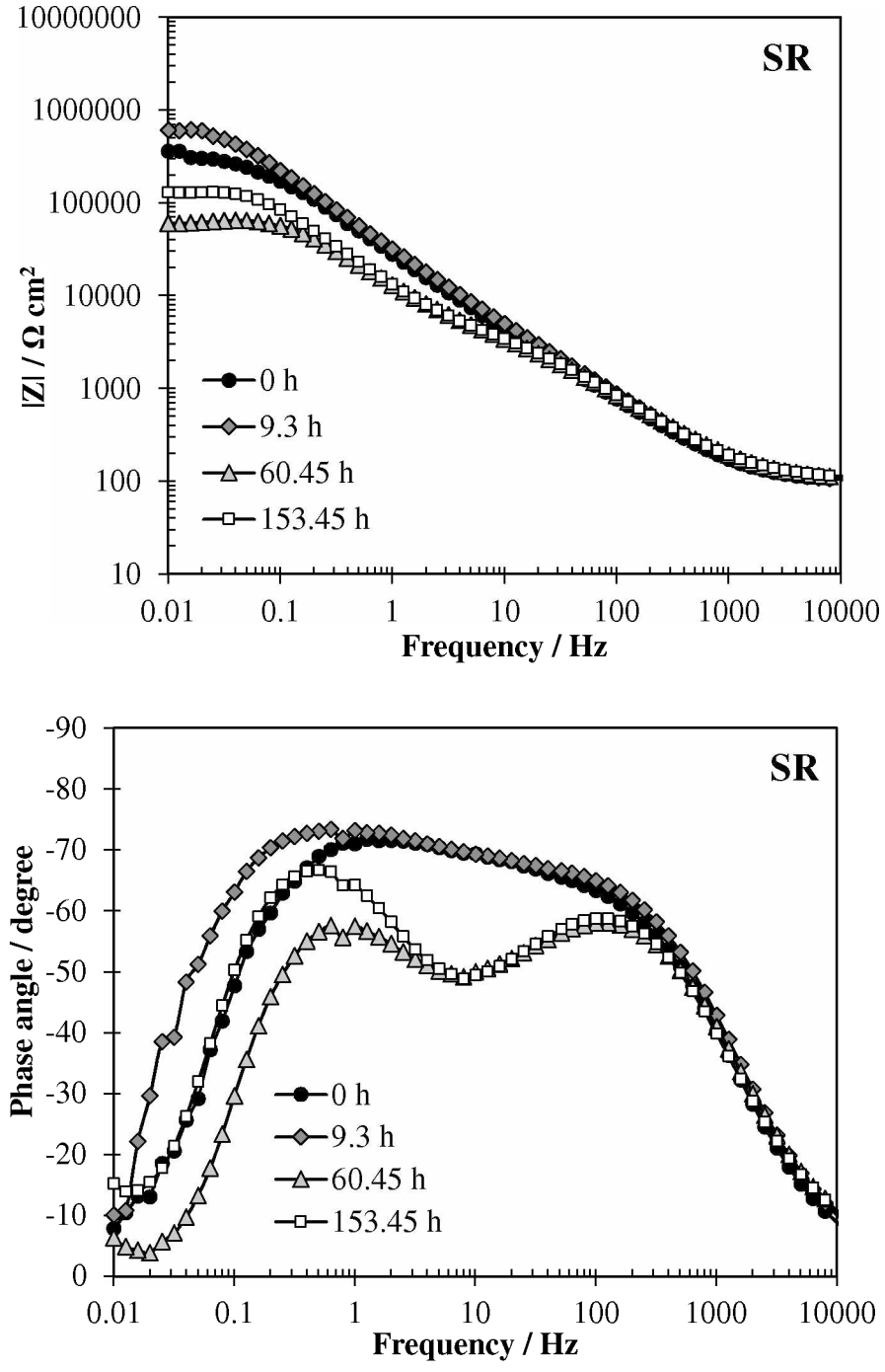

Figure 9 Effect of exposure time on EIS Bode plots of SR specimens, on P surface, in aerated Harrison solution

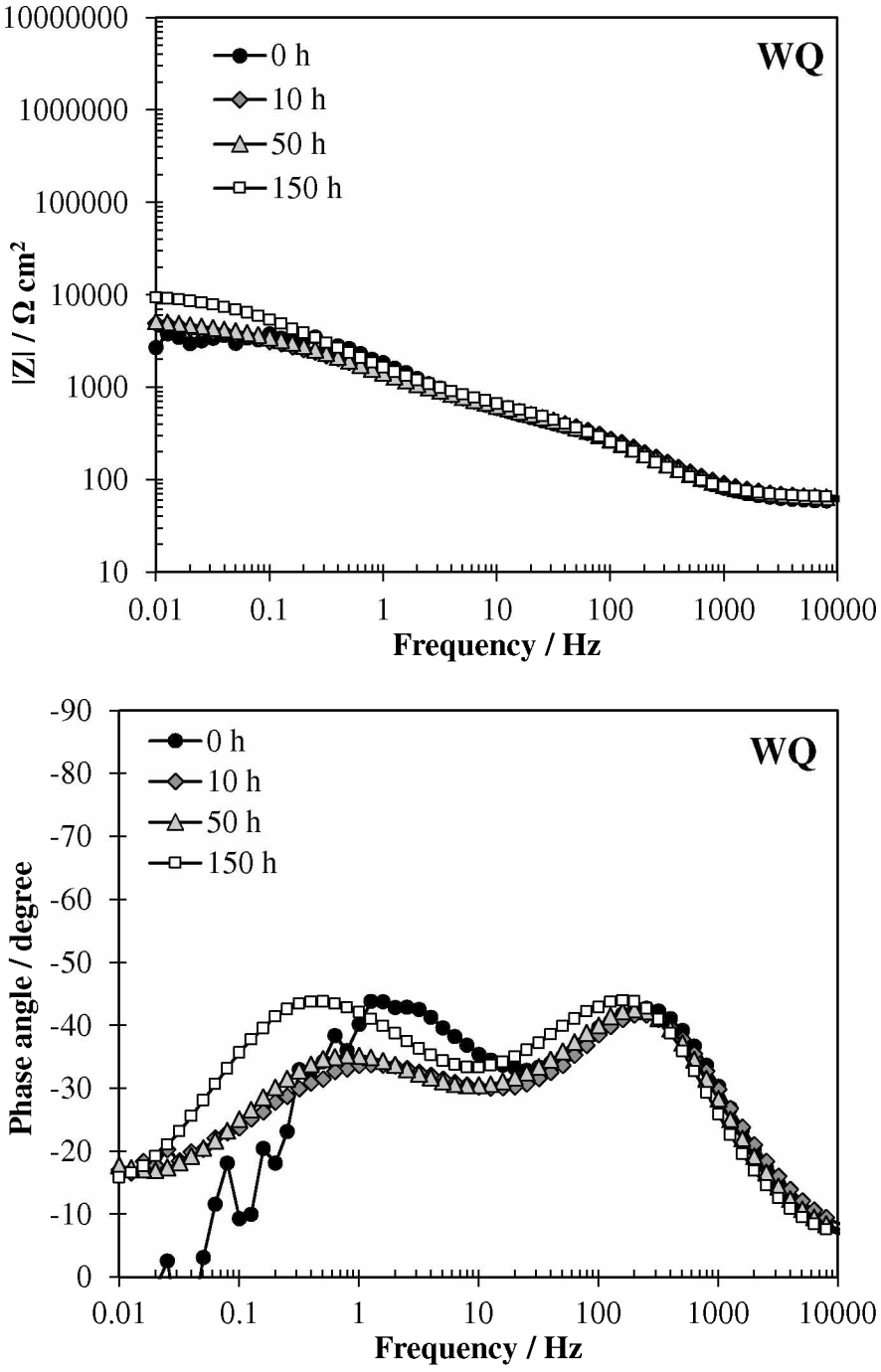

Figure 10 Effect of exposure time on EIS Bode plots of WQ specimens, on P surface, in aerated Harrison solution

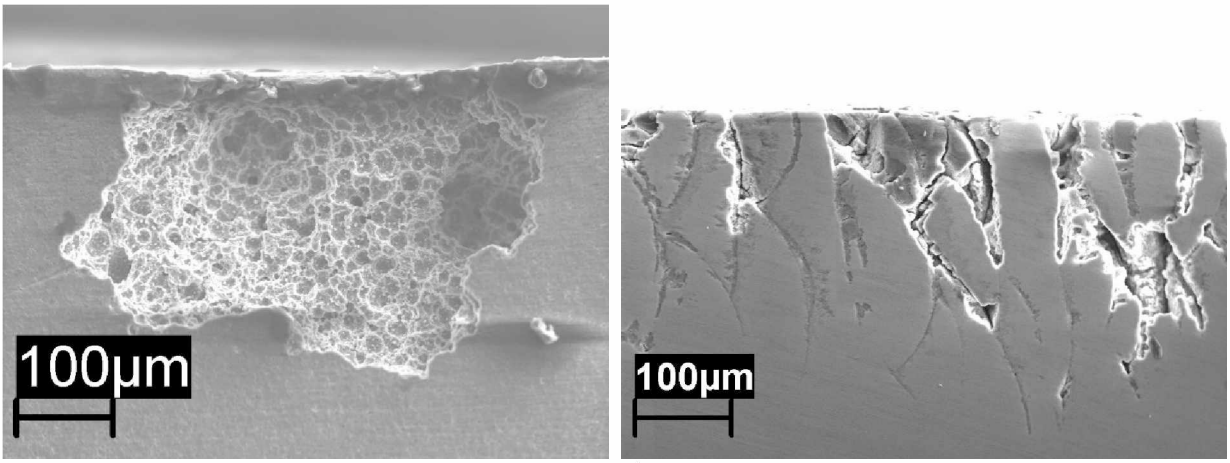

a) b)

Figure 11: SEM images of metallographic section. Corrosion morphology after long exposure in Harrison solution: a) pitting on WQ specimens, b) selective penetrating attack on UT specimen

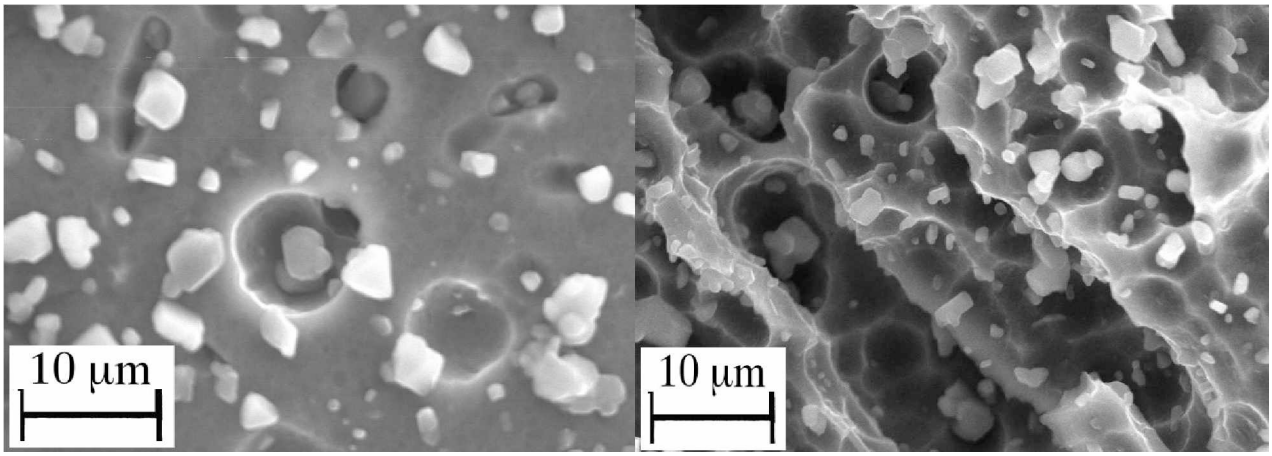

Figure 12: Corrosion morphology on WQ specimens after 300 hours exposure in Harrison solution

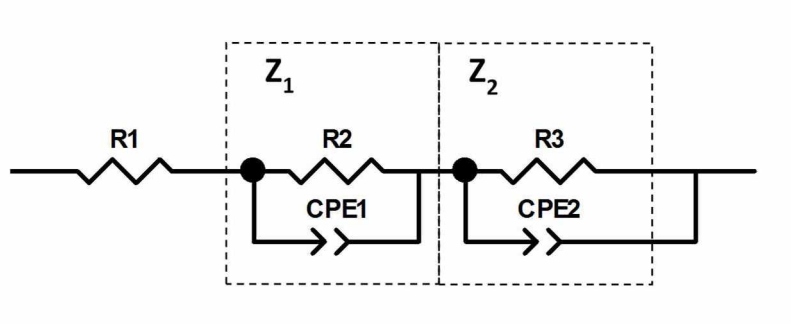

Figure 13 Simplified equivalent circuit suitable to decribe EIS spectra evolution over time

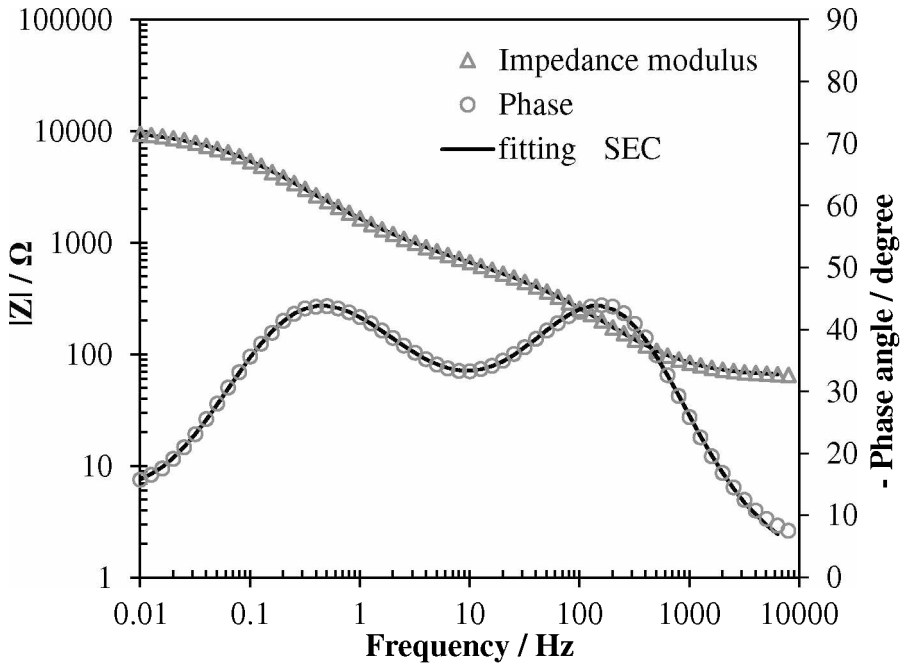

Figure 14: Fitting of experimental data by applying the SEC on WQ specimen

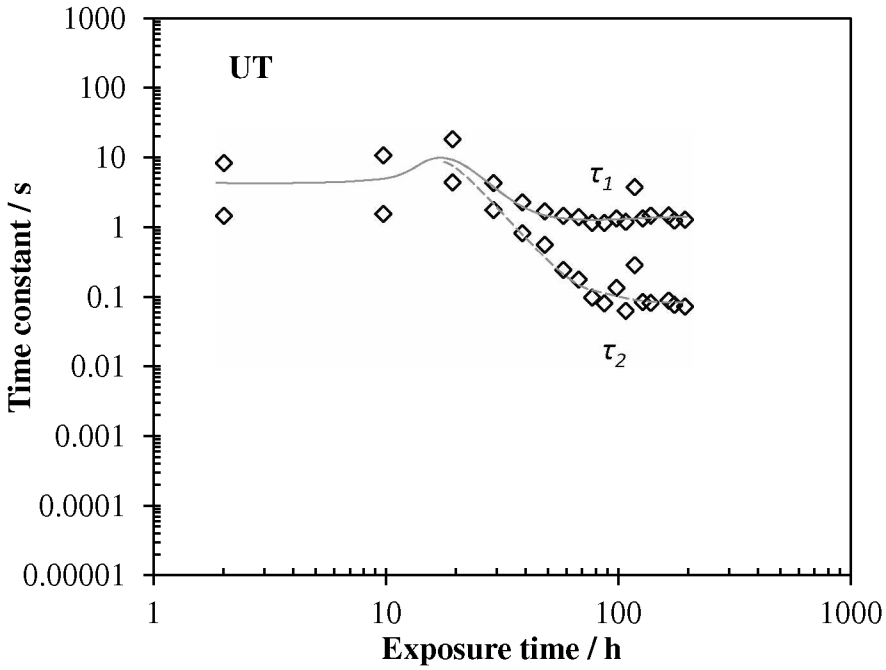
UT
Time constant / s
Exposure time / h
1000
100
10
1
0.1
0.01
0.001
0.0001
0.00001
1
10
100
1000
τ_1
τ_2

a)

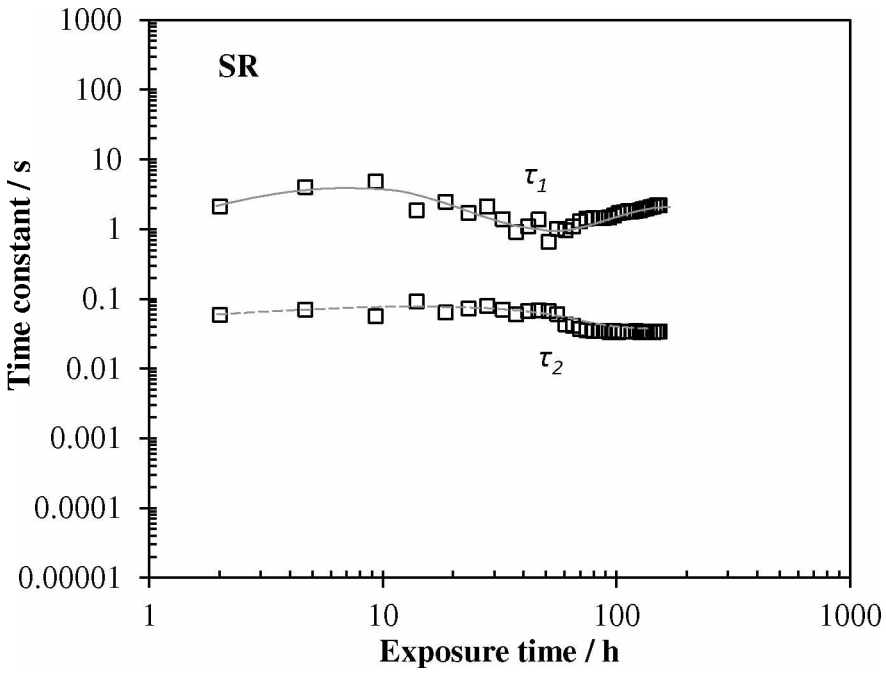
SR
Time constant / s
Exposure time / h
1000
100
10
1
0.1
0.01
0.001
0.0001
0.00001
1
10
100
1000
τ_1
τ_2

b)

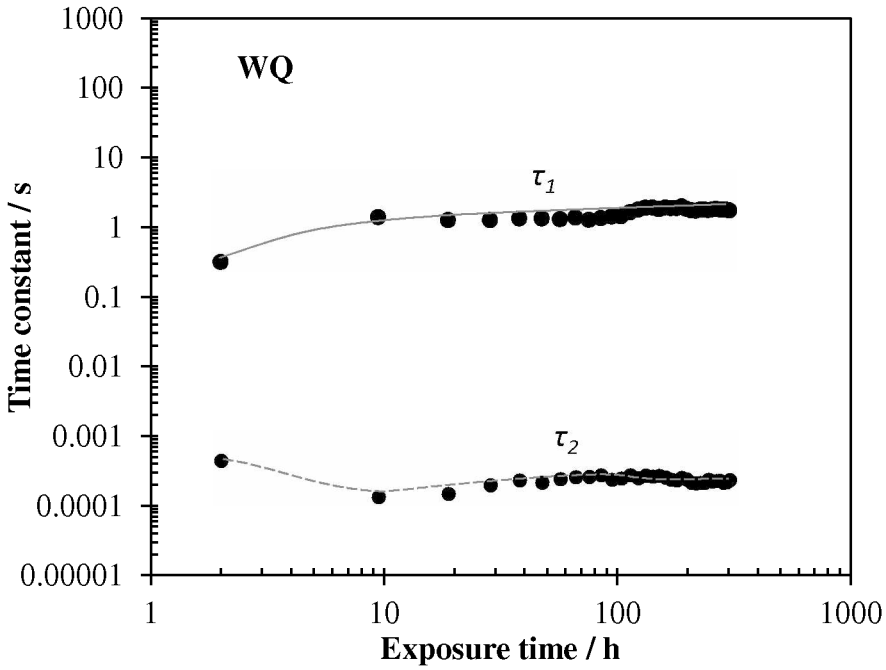

c)

Figure 15: Time constant evolution as a function of exposure time derived from EIS data fitting by means of SEC on a) UT, b) SR, c) WQ specimens